Determination of the intensity/energy response function of a hemispherical photoelectron analyser based on Tougaard background

Stéphane Guilet, Léa Bataillou, Rémi Lazzari, Olivier Kerivel

Determination of the intensity/energy response function of a hemispherical photoelectron analyser based on Tougaard background

Stéphane Guilet[1], Léa Bataillou[1], Olivier Kerivel[1], Rémi Lazzari[1,*]

[a] *CNRS, Sorbonne Université, Institut des NanoSciences de Paris, UMR 7588, 4 Place Jussieu, F-75005 Paris, France*

Abstract

A new method is proposed for the determination of the intensity/energy response function of a hemispherical electrostatic analyser as commonly used in photoemission spectroscopy. It only requires the measurement of a wide spectrum of a reference metallic sample. Based only on the knowledge of the Tougaard inelastic electron scattering cross section and an educated parametrization of the response function, the retrieval algorithm minimizes the area of the background subtracted primary spectrum with some constraints. Sound results for different metals (Ag, Au, Cu, Zn) are obtained (i) on two different photoemission instruments (ii) in both fixed analyser transmission and fixed retarding ratio modes (iii) for various lens and slits settings (iv) for both monochromated and unmonochromated x-ray sources. The linear correlation between core level areas and the product of tabulated inelastic mean free paths and of photo-ionisation cross sections validates the approach.

Keywords: photoemission, Tougaard background, hemispherical analyser, transmission function

1. Introduction

Photoemission spectroscopy [1], most of the time performed with a concentric hemispherical electron analyser, is a key tool for the analysis of chemical states of elements not only in surface science but more generally in material characterisation. Binding energies of core levels or kinetic energies of Auger transitions provide characteristic fingerprints of elements but also of their chemical environment via shifts in energies. Besides this chemical analysis capability, the concentrations of probed elements can be assessed by comparing relative intensities of recorded features. Accuracies down to a fraction of a percent in the bulk or in coverage for a deposit can be reached [2]. Quantification is obtained via a well-established formalism of straight electron trajectory [1, 3–6] for which the elastic intensity $I_i(E_K)$ of a core level i at kinetic energy E_K for an element in a matrix m is given by:

$$\begin{aligned} I_i(E_K) &\propto \Phi \frac{d\sigma}{d\Omega} \Delta\Omega T_F(E_K) A(E_K) D(E_p) \\ &\times \int_0^{+\infty} n_i(z) \exp\left(-\frac{z}{\lambda_{im}(E_K)\cos\theta}\right) dz, \end{aligned} \tag{1}$$

where Φ is the incident flux of x-rays photons of energy $h\nu$, $\frac{d\sigma}{d\Omega}$ is the differential photo-ionisation cross section, $\Delta\Omega$ is the acceptance angle of the analyser, $T_F(E_K)$ is the total transmission function of the focusing/retardation electrostatic column and of the analyser, $A(E_K)$ is the convolution between the area irradiated by the x-ray source and the area analysed by the spectrometer (see Ref. [7] for details), $D(E_p)$ is the detector efficiency at the used pass energy E_p, $n_i(z)$ is the element concentration at depth z, $\lambda_{im}(E_K)$ is the inelastic mean free path of core level i in the matrix m and θ is the emission angle between the surface normal and the analyser. $\frac{d\sigma}{d\Omega} = \sigma_i^*(h\nu, E_K) W_i(h\nu, E_K, \theta_X)$ is given by the product of the photo-ionisation cross section of the considered core level $\sigma_i^*(h\nu, E_K)$ and of the anisotropy factor of the latter $W_i(h\nu, E_K, \theta_X)$ which depends on the angle θ_X between the x-ray source and the analyser. For unpolarized radiation, $W_i(h\nu, E_K, \theta_X) = \frac{1}{4\pi}\left[1 - \frac{\beta}{4}(3\cos^2\theta_X - 1\right]$ where $\beta(h\nu, E_K)$ is an asymmetry parameter. Elastic scattering effects can be reintroduced in Eq. 1 through a modified cross section $\frac{d\sigma}{d\Omega}$ or by replacing properly in the quantification the inelastic mean free path by the effective attenuation length (see [4, 5, 8, 9] for details). In fact, the splitting in Eq. 1 of the intensity energy response function of the apparatus (or étendue) as a product $R_F(E_K) = \Delta\Omega T_F(E_K) A(E_K)$ is already a simplification as the acceptance angle of the analyser and the irradiation may vary with the position across the sample surface [10–13]. For a constant concentration profile that is to say a bulk homogeneous material, the integral in Eq. 1 reduces to $n_i \lambda_{im}(E_K)\cos\theta$. Eq. 1 ignores photo-diffraction effects and is more suited for polycrystalline or ill-crystallized samples. It involves parameters that are calculated or tabulated [$\sigma_i^*(h\nu, E_K)$

*Corresponding author

Email addresses: stephane.guilet@insp.jussieu.fr (Stéphane Guilet), lea.bataillou@insp.jussieu.fr (Léa Bataillou), olivier.kerivel@insp.jussieu.fr (Olivier Kerivel), remi.lazzari@insp.jussieu.fr (Rémi Lazzari)

and $W_i(h\nu, E_K, \theta_X)$ [14–16], $\lambda_{im}(E_K)$ [17–22]] and others that are related to the instrument and the geometry of measurement [Φ, $D(E_p)$, $T_F(E_K)$, $A(E_K)$, θ_X, θ]. Since absolute intensity measurements are impossible, information about the concentration of an element is usually obtained through ratios of core level peak areas using a reference core level of the matrix. At constant x-ray flux, pass energy and angles, the remaining unknown in the quantification is then the intensity/energy response function of the apparatus $R_F(E_K)$ that plays a paramount role when comparing results obtained from different spectrometers [7, 11, 23]. Therefore poor results in terms of quantification may be obtained when using general empirical databases of relative sensitivity factors [24] if $R_F(E_K)$ is not properly accounted for.

For a concentric hemispherical photoemission analyser, $T_F(E_K) = L_F(E_K)H_F(E_K)$ can be decomposed into the contributions [23, 25] (i) of the input lens column $L_F(E_K)$ that combines the focusing and retardation lenses and (ii) of the concentric hemisphere itself $H_F(E_K)$. While the pass energy E_p drives the resolution ΔE_K, $H_F(E_K)$ scales with E_p and therefore depends on the selected working mode. In the fixed analyser transmission (FAT) mode at fixed E_p and therefore fixed ΔE_K as commonly used in photoemission, $H_F(E_K)$ is constant. In the fixed retardation ratio (FRR) mode for which the ratio $R = E_K/E_p$ (and also the relative resolution $\Delta E_K/E_K$) is constant, $H_F(E_K)$ scales as $1/E_K$ [1]. The FRR mode is preferred for Auger spectroscopy to enhance transmission at low kinetic energy. In the absence of paraxial aberrations, as the entry angles of the hemisphere are fixed and thus determine the exit angles from the input lens, $L_F(E_K)$ can be directly derived from the Abbe sine condition of optics (or Helmholtz-Lagrange in electron optics) [13, 23, 25, 27] for a fixed magnification. In FAT mode, $L_F(E_K)$ follows a $1/E_K$ trend while in FRR mode, it is constant. Combining the transmissions of both elements $L_F(E_K)$ and $H_F(E_K)$, an aberration-free or perfect analyser behaves as $T_F^{FAT}(E_K) \propto 1/E_K$ in FAT mode and as $T_F^{FRR}(E_K) \propto E_K$ in FRR mode. However, a real apparatus through the lens settings and the presence of various apertures to define the beam exhibits all kinds of aberrations, not speaking about internal electron scattering [28], and therefore deviates from this theoretical behaviour [11–13, 23, 25–27, 29–37]. Moreover, using a scanning electron gun as a point source for imaging, Mahjoub *et al.* [13] demonstrated that, at variance to common assumptions in photoemission quantification, the area probed by the analyser does depend on kinetic energy even with an unmonochromated non-focused source. Added to the convolution between the sample size and irradiated area in $A(E_K)$, this leads to a global apparatus response that is different from the transmission function of the analyser itself [7].

Besides a complete and complex simulation of electron ray tracing for a given apparatus design [12, 36] (that is often unfortunately proprietary!), several experimental and practical calibration methods [7, 11, 23, 25–27, 30, 34–36, 36–39] have put forward to determine $R_F(E_K)$, (often mixed up with $T_F(E_K)$) leading still to a power law trend in FAT mode.

Cross and Castle [25] proposed to make the intensity ratio $I_{FAT}(E_K)/I_{FRR}(E_K)$ of spectra acquired in FAT and FRR modes to get rid off of the sample peaks and to reveal the apparatus transmission function. For an ideal analyser, $I_{FAT}(E_K)/I_{FRR}(E_K) \propto 1/E_K^2$. By assigning most of the optical aberrations to the transmission function in FAT mode via an exponent $T_F^{FAT}(E_K) \propto 1/E_K^{\alpha}$, the fit of the ratio $I_{FAT}(E_K)/I_{FRR}(E_K)$ gives directly α. Nevertheless, the underlying assumption of $T_F^{FRR}(E_K) \propto E_K$ remains not clearly justified [30]. This methodology was applied by Ruffieux *et al.* [34] to an analyser similar to one tested herein. They found a nearly ideal behaviour with $\alpha \simeq 1$ but only on restricted ranges of kinetic energies [34].

Based on tabulated photo-ionisation cross sections and inelastic mean free paths, Eq. 1 can also be used to determine the analyser response function for known reference samples [26, 27, 35, 36]. Besides inherent uncertainties in the databases used [4, 21] and the question of contamination, there are drawbacks of this "first-principle" method (also called Quantified Peak Area Approach, QPA). Firstly, the $R_F(E_K)$ function is only sampled at the available kinetic energies of the studied material core levels, thus requiring many reference samples usually metals but also ionic liquids [40]) an *ad hoc* interpolation function. Secondly, the zero loss line areas in particular for small intensity peaks [41, 42] are quite sensitive to the background used to derive them.

True photoemission spectra (*i.e.* absolute spectra with all instrumental terms removed) of clean sputtered coinage metals such as Ag, Au, Cu are also available to calibrate a given instrument [7, 11, 23, 35, 36, 38]. But this procedure (the so-called Survey Spectra Approach, SSA) requires a spectrum of a clean reference material measured with the same excitation source and with similar experimental geometry and resolution to minimise issues related to the spectra ratio. If an ion gun is not available to clean the sample but a charge compensation tool is, low-density polyethylene turned also to be a good candidate for such a calibration method due its large background and few intense features, but at the expense of longer acquisition times and of dark noise measurement [37, 39].

Beyond the ability to polarise the sample, the bias method [30, 33] requires measurements at different voltages on signal background. It assumes that the additional electric field due to the polarised sample manipulator has

[1] As the detector efficiency poorly depends on pass energy for commonly used values if the counting rate is not too high, it does not contribute to the overall transmission of the analyser itself even in FRR mode [26]. Of course, in FAT mode, this latter is constant.

a negligible impact on the transmission function. Based on the Liouville theorem applied to the propagation of charged particles, Triguiero *et al.* [27] proposed also to determine a correction function by biasing the sample at much higher voltage to shift one core level to the kinetic of an other one prior to measure the transmission function at any kinetic energy. Still, the method relies on some tabulated parameters [$\sigma^*(E_K)$ and $\lambda(E_K)$] and peak intensity integration.
Other authors exploited the dependence of the background signal in pass energy at constant kinetic energy to deduce the exponent α of the transmission function in FAT mode [26, 31, 32]. But this assumes a separable relationship between both variables and that the detector efficiency or the electron scattering inside the concentric hemispherical analyser [28] do not change with pass energy.

Most of the proposed calibration methods are either time consuming, rely on restrictive assumptions or require some instrumental specificity. In the present paper, an algorithm for retrieval of the analyser intensity/energy response function is developed using the inelastic background of a wide spectrum. Aside the inelastic electron scattering cross section, the method does not require any tabulated data, true spectrum or polarisation; experimentally, the measurement is performed only on a clean metallic polycrystalline reference (such as Ag) as often already present in any photoemission setup for calibration purposes.

The article is organised as follows. After an experimental part (Sect. 2), the underlying concepts of the algorithm are detailed in Sect. 3. After a test on simulated data (Sect. 4.1), it is then applied successfully in Sects. 4.2-4.3 to actual measurements on various metals with two different analysers working in the two usual acquisition FAT and FRR modes. The approach is finally validated against tabulated relative sensitivity factors (Sect. 4.4).

2. Experimental

Experiments have been performed on two different vacuum vessels involving two different photoemission apparatuses (base pressures in the low 10^{-10} mbar). The first one involves a 125 mm radius hemispherical analyser (EA-125 from ScientaOmicron [43]) combined with a 5 channeltron detector and a dual Al/Mg-Kα unmonochromated x-ray source (DAR400 from ScientaOmicron). Two sets of slits of circular or rectangular shape can be selected, either at the entrance of the hemisphere (6×12 mm^2, $\phi = 6$ mm, $\phi = 2$ mm, $\phi = 1$ mm, 1×12 mm^2) or in front of the detector (1×10 mm^2, 3×10 mm^2, 5×11 mm^2). The second setup is based on a 100 mm radius analyser (Phoibos-100 from SPECS [44]) associated with a delay-line detector and an Al-Kα monochromated x-ray source (XM1000 from ScientaOmicron). Beside a similar set of slits (entrance: 0.2×20 mm^2, 0.5×20 mm^2, 1×20 mm^2, 3×20 mm^2, 7×20 mm^2, $\phi = 1$ mm, $\phi = 3$ mm, $\phi = 7$ mm; exit : 0.3×20 mm^2, fully open with/without a mesh), an iris in the middle of the input optical column can be varied between 2.5 and 50 mm to suppress the most aberrated electron trajectories; it was kept open at 15 mm for all measurements. This function is insured in the EA-125 machine by a fixed aperture. The angle between source and EA-125 analyser corresponds to the magic value $\theta_X = 54.7°$ at which the asymmetry factor effect in the photo-ionisation cross section vanishes, while the monochromator flange on the Phoibos-100 chamber is at $\theta_X = 35°$. On both analysers, angular acceptance and therefore analysed area can be varied with the preselected electron optics magnification mode [34]. Finally, both input lens columns can work (i) in FAT mode at fixed pass energy or (ii) in the FRR mode for which the ratio $R = E_K/E_p$ is kept constant. Combining the choice of the excitation source, the large set of slits, the magnification and working modes, the intensity response in kinetic energy of the whole measurement chain can be varied over a large range, not speaking about the linearity of the detector or the choice of the collection angle θ.

In the present study, all measurements have been performed in a normal ($\theta = 0°$ for EA-125) or close to normal ($\theta = 35°$ for Phoibos-100) emission configuration either in FAT or FRR modes with Al-Kα excitation ($h\nu = 1486.6$ eV). Spatially resolved mode with an acceptance area limited by the input lenses (high magnification mode on EA-125) was selected for most measurements with the unmonochromated source while transmission was favoured with the smaller monochromated beam footprint (medium area mode for Phoibos-100). Only wide scans have been recorded for kinetic energies (E_K) ranging between ~ 100 eV and ~ 1470 eV. A pass energy of 50 eV for EA-125 and 20-50 eV for Phoibos-100 was chosen since resolution is not an issue herein; in FRR mode, the retardation ratio was adapted to have a similar counting rate as in FAT mode for the most intense core level while achieving reasonable E_p at the smallest E_K. The pass energy should be large enough to avoid internal scattering in the hemisphere and a spurious increase of the background signal [28]. Finally, caution was taken to measure at kinetic energies above the photon excitation for a good estimate of the initial background. At the opposite, the kinetic energy range below 100 eV was not recorded to avoid detector non-linearity due to the burst of secondary electrons in FAT mode and to have a reasonable counting rate in FRR mode. Moreover, beyond the lack on interesting spectroscopic features for most materials at such energies, the trajectories of those slow electrons are more sensitive to any disturbance such as magnetic fields. Also the chosen energy step was small enough ($\Delta E = 0.05 - 0.3$ eV) to insure an accurate numerical integration in the inelastic background (Eq. 2)

and the peak areas.

Polycrystalline high-purity samples of about 1 cm^2 of Ag, Cu, Au and Zn were prepared by Ar^+-sputtering (beam energy 1 keV, current of $\sim 10\,\mu A$) until the contamination level by carbonaceous species and oxide was below the detection limit on a wide scan. The obvious advantage of those metals is their conductivity and their relative inertness under vacuum once prepared.

3. Response function from Tougaard background: the algorithm

Let's call $S(E_K)$ the primary spectrum of emitted electrons upon x-ray irradiation. Upon their path to the surface, the electrons will suffer from inelastic collisions leading to a distorted signal $M(E_K) = S(E_K) + B(E_K)$ associated to an extrinsic background $B(E_K)$. For a homogeneous distribution of emitters, the background can be accounted for via a integral equation [45–48] involving a kernel $\mathcal{K}(E_K, T)$ corresponding to the probability per unit of length of an energy loss $T = E'_K - E_K$ for an electron of kinetic energy E_K :

$$B(E_K) = \int_{E_K}^{+\infty} \lambda(E_K)\mathcal{K}(E_K, E'_K - E_K)M(E'_K)dE'_K, \quad (2)$$

where $\lambda(E_K)$ is the inelastic mean free path. Note $B(E_K)$ accounts intrinsically for multiple losses via the presence of the $M(E'_K)$ term in the integral. Theoretically $\mathcal{K}(E_K, T)$ is related to an integral of the non local loss function of the considered material. Fortunately, the product $\lambda(E_K)\mathcal{K}(E_K, T)$ depends strongly on energy loss T but moderately on the material and on the kinetic energy E_K. In fact, finer details are smeared out by the convolution with the intrinsic peak width, experimental resolution and multiple scattering events [46]. For metals, their oxides and alloys, Tougaard demonstrated that the product can be conveniently described by the following two/three parameter functions [46–49]:

$$\begin{aligned} \lambda(E_K)\mathcal{K}(E_K, T)) &= \frac{B(T-G)\Theta_H(T-G)}{[C + (T-G)^2]^2} \quad (3) \\ \lambda(E_K)\mathcal{K}(E_K, T) &= \frac{B(T-G)\Theta_H(T-G)}{[C - (T-G)^2]^2 + D(T-G)^2}, \end{aligned}$$

where B, C, D are material dependent parameters, G the corresponding band gap and $\Theta(T)$ the Heaviside function ($\Theta(T) = 0$ for $T < 0$; $\Theta(T) = 1$ for $T > 0$). The values of the parameters were determined theoretically from extensive dielectric calculations or experimentally from reflection energy loss spectroscopy [47]. For most materials, the so-called universal cross section (Eq. 3) with $C = 1643$ eV^2 and $B \simeq 3000$ eV^2 provides sound results [47, 50] but can be refined to include intrinsic losses due to the sudden creation of the hole during the photo-excitation process [51]. Depending on the width of the cross section, more accurate results can be obtained with the three-parameter function in particular in the presence of narrow plasmon structure. Note that the Tougaard background (Eq. 2) is independent of the nature of the primary electron (that is to say core level or Auger transitions) and is linearly additive and therefore valid for a polychromatic excitation (*i.e.* for satellites and Bremsstrahlung emission of an unmonochromated source). With usual parameters, the background extends over several tens of electron volts above the primary spectrum peak meanwhile, whatever the peak line shape, this latter tend towards zero. If the response function of the analyser is known, the Tougaard background was shown to be better suited in terms of quantification compared to Shirley or linear backgrounds although it does not account for intrinsic losses [42, 52–54].

Based on these observations, an iterative algorithm to recover the response function in kinetic energy $R_F(E_K)$ can be devised from a simple wide spectrum of a flat homogeneous sample. Its flow chart is sketched in Fig. 1. Starting from an actual measured spectrum $I(E_K) = R_F(E_K)M(E_K)$, at iteration k, a trial total spectrum $M^{(k)}(E_K)$ is obtained by dividing $I(E_K)$ with an initial educated and sound estimate of $R_F^{(k)}[E_K, \alpha(E_K)]$ that depends on a limited number of parameters within $\alpha(E_K)$ (see below). From $M^{(k)}(E_K)$, an estimate of the background $B^{(k)}(E_K)$ is then obtained using Eq. 2 with the most suitable two or three parameters cross section (Eqs. 3) for the considered material. To obtain $R_F(E_K)$, the process is iterated for a new parameter set in $\alpha(E_K)$ until the area $\mathcal{A}_k(\alpha)$ under $S^{(k)}(E_K) = M^{(k)}(E_K) - B^{(k)}(E_K)$ is minimal. The idea is that, over a large fraction of the total spectrum $M(E_K) = S(E_K) + B(E_K)$ in between core level peaks or Auger lines, the spectrum overlaps with its background leading to a primary spectrum $S(E_K)$ of minimal area (see for example Fig. 2). Beyond this assumption, the algorithm is based on the validity of the Tougaard background to grasp the right $B(E_K)$ line shape. If some discrepancies might appear close to the primary peak, it was already demonstrated that Eqs. 2-3, in particular for bulk metals, give a fair estimate in a kinetic energy range of a few tens of electron-volts below photoemission lines [47] since multiple scattering events undergone by electrons smooth out the exact details of the cross section of energy loss.

In the present case, the analysis was limited to coinage or late transition metals (Ag, Au, Cu, Zn) for which the three-parameters cross section (Eq. 3) gives the most accurate results with $B = 4200$ eV^2, $C = 1000$ eV^2, $D = 13300$ eV^2, $G = 0$ eV. If not stated, these values were used all along this work. Deviations from the $1/E_K$ and E_K behaviour of the perfect analyser in FAT and FRR modes respectively were accounted for by power laws [7, 26]:

$$R_F^{FAT}(E_K) = 1/E_K^{\alpha(E_K)}$$

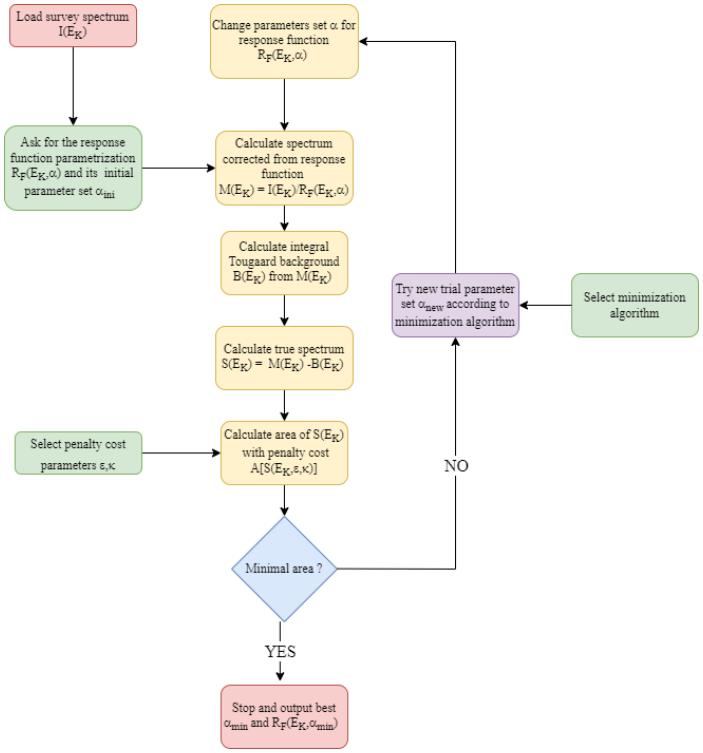

Figure 1: Flow chart of the proposed algorithm of response function retrieval.

$$R_F^{FRR}(E_K) \;=\; E_K^{\beta(E_K)}, \tag{4}$$

where the exponents are polynomial functions of E_K:

$$\begin{aligned} \alpha(E_K) &= \sum_{i=0}^{n_\alpha} \alpha_i \left(\frac{E_K}{1000}\right)^i \\ \beta(E_K) &= \sum_{i=0}^{n_\beta} \beta_i \left(\frac{E_K}{1000}\right)^i . \end{aligned} \tag{5}$$

To further constraint the optimisation and to better describe the actual behaviour of $R_F(E_K)$ with a transition between two nearly constant exponent values (see below), the following effective dependence was also adopted for both exponents $\alpha(E_K)$ and $\beta(E_K)$:

$$\begin{aligned} \alpha(E_K) &= \widetilde{\alpha} + \Delta\alpha \,\mathrm{Erf}\left[\frac{E_K - E^0_{K,\alpha}}{\Delta E_{K,\alpha}}\right] \\ \beta(E_K) &= \widetilde{\beta} + \Delta\beta \,\mathrm{Erf}\left[\frac{E_K - E^0_{K,\beta}}{\Delta E_{K,\beta}}\right], \end{aligned} \tag{6}$$

where $\mathrm{Erf}(E) = \frac{2}{\pi}\int_{-\infty}^{E} e^{-t^2} dt$ is the error function. To avoid convergence toward irrelevant and unphysical solutions with negative intensity $S^{(k)}(E_K)$ values, the minimized cost function $\mathcal{A}_k(\alpha)$ was chosen as the area of the absolute value of $S^{(k)}(E_K)$ instead of its actual area. Also to favour the overlap between $B^{(k)}(E_K)$ and $M^{(k)}(E_K)$ over the largest range of energy while accounting for the inherent noise in measurement, a penalty cost controlled by the ϵ and κ parameters was introduced:

$$\mathcal{A}_k(\alpha) = \frac{1}{\epsilon + \omega_k} \int |S_k(E_K)|\, dE_K, \tag{7}$$

where $0 \leq \omega_k \leq 1$ is the fraction of kinetic energies where $|S_k(E_K)|$ is close to zero within the measurement noise $N(E_K)$ *i.e.* $|S_k(E_K)| < \kappa N(E_K)$. Assuming a shot noise with a Poisson statistics, a good estimate is given by $N(E_K) \simeq \sqrt{I(E_K)}$ with $\kappa \simeq 1$. For $\epsilon \ll \omega_k < 1$, the cost function strongly disadvantages unphysical solutions for which $\omega_k \simeq 0$ or the response function blows up and the intensity goes towards zero. At the opposite limit for $\epsilon \gg 1 > \omega_k$, only the area is really minimized. Noise needs to be accounted for only in $S_k(E_K)$ since the integral in Eq. 2 intrinsically performs a smoothing in $B_k(E_K)$. Caution was taken to measure spectra well above the maximum kinetic energy E_K^m of the Kα emission line of the source so that, above, one can assume no signal despite the bremsstrahlung excitation *i.e.* $M(E_K) = S(E_K) = B(E_K) = 0$. In practice, the integral of Eq. 2 is then evaluated between E_K and E_K^m for $M^*(E_K) = M(E_K) - M(E_K^m)$.

The algorithm was implemented in the *Igor Pro Paris Photoemission Package* [55]. To speed up calculation, $B(E_K)$ (Eq. 2) was calculated via convolution in Fourier space. The minimization of the cost function was performed with the *Optimize* function of *Igor Pro* [56] based on the line search, the dogleg trust region method or the hookstep trust region method of More-Hebdon algorithm [57]. The minimization was converged until predefined relative tolerances ($\sim 10^{-4}$) on the gradient of the function and on the minimization step length. In ill-conditioned cases too far from the actual solution, the loop (Fig. 1) is stopped after a given number of iterations (~ 100) before being launched from a new trial starting point. Search with the Corana algorithm of simulated annealing [58] was also implemented for a more global search of minimum.

4. Results

4.1. Algorithm test on a simulated spectrum

First of all, the algorithm was intensively tested on a simulated wide spectrum of Ag at fixed resolution with a known response function $R_F(E_K) = 1/E_K$ *i.e.* $\alpha(E_K) = \alpha_0 = 1$ (Fig. 2). The primary spectrum $S(E_K)$ was calculated at $h\nu = 1486.6$ eV as a sum of asymmetric core level peaks of similar width (asymmetric Voigt functions with gaussian and lorentzian full-widths at half maximum of 0.5 and 1.5 eV respectively) at tabulated metallic binding energies, spin orbit splittings and areas [59–61]. As expected for a semi-infinite homogeneous material, the latter were taken as the product of the calculated photoionisation cross sections $\sigma^*(h\nu, E_K)$ [15] and the TPP-2M

inelastic mean path $\lambda(E_K)$ [17, 22]. Auger lines and valence band were mimicked by gaussian peaks which intensities and broadenings were taken close to experimental ones (see Fig. 5(a)). From this simulated $S(E_K)$, the Tougaard background $B(E_K)$ was then calculated iteratively using Eqs. 2-3 with $B = 4200$ eV^2, $C = 1000$ eV^2, $D = 13300$ eV^2, $G = 0$ eV down to a relative accuracy of 0.005. Their sum $M(E_K) = S(E_K) + B(E_K)$ was then multiplied by the selected response function $R_F(E_K) = 1/E_K$ to obtain $I(E_K)$. Finally, the overall intensity was scaled to match the typical experimental counting rate before adding a Poisson noise with a variance equal to $I(E_K)$.

Fig. 2 illustrates the ability of the method to recover exactly the initial response function with a standard algorithm of smart steepest descent (red versus black dotted lines). As shown in Fig. 3(a) for a constant $\alpha(E_K) = \alpha_0$ (Eq. 5), the proposed penalty of the cost function $\mathcal{A}_k(\alpha)$ (Eq. 7) helps distorting favourably the concavity of the one-dimensional parameter space compared to a simple criterion based on the area (blue curve with $\epsilon = 100$ versus green/red curves with $\epsilon = 0.001$). The minimization can be even more constrained towards the actual solution by decreasing the κ value (green curve $\kappa = 0.5$ versus red curve $\kappa = 1$). A polynomial exponent up to order four ($n_\alpha = 4$ in Eq. 5) was then tested in the retrieval process leading to the same type of accuracy as defined by the curvature matrix of $\mathcal{A}(\alpha)$ close to the minimum (not shown). Nevertheless, as for any minimization process, the main drawback is the convergence towards local minima that do not lead to large kinetic energy ranges where $S(E_K)$ is close to zero. In this respect, simulated annealing can be of help but at the expense of calculation cost (tens of minutes compared to a few seconds on a standard computer).

Using the same theoretical curve (Fig. 2), the sensitivity of the algorithm to the parameters of the inelastic electron scattering cross section (Eq. 3) was then tested by varying the $[B, C]$ values by ± 20 % or by changing the gap to 2.5 eV (Fig. 3(c)). Provided that the cross section is normalised to the same area via the $B-$parameter [47], the optimal α_0 value is found within less than 0.07 from the nominal one (Fig. 3(b)). This finding illustrates the poor dependence of method to the exact shape of the cross section in the primary peak region. By overweighting the matching between $M(E_K)$ and $B(E_K)$, the algorithm is more sensitive to the global power law decay of the cross section a few tens of electron-volts below the zero-loss line.

4.2. Response function parametrization

Before testing the algorithm on actual spectra of clean metal foils, the question of the arbitrariness of the parametrization of the response function was first tackled by looking at the ratio of spectra acquired in FAT and FRR modes with similar slits and magnification condition. For a perfect analyser, $I_{FAT}(E_K)/I_{FRR}(E_K)$ should scale with $1/E_K^2$ while in the general case, a trend in $1/E_K^{\alpha(E_K)+\beta(E_K)}$ is expected. As shown in Fig. 4, depending on the chosen apparatus configuration, the ratio $\mathcal{R}(E_K) = E_K^2 I_{FAT}(E_K)/I_{FRR}(E_K)$ can deviate substantially from a perfect constant behaviour (dotted line in Fig. 4). This was already pointed out in Refs. [13, 34] for the same EA-125 analyser. Excluding the low kinetic energy range $E_K \lesssim 250$ eV where the trend is complex (shaded area in Fig. 4), curves can be gathered in two groups for the EA-125 analyser: (A) a nearly perfect behaviour with a $\alpha(E_K) + \beta(E_K) - 2$ value close to zero or slightly negative and (B) a nearly symmetric change of $2 - \alpha(E_K) - \beta(E_K)$ slope from a positive to a negative value at $E_K \simeq 800$ eV over a with of ~ 200 eV. Regarding the Phoibos-100 apparatus, similar curves show two changes of positive $2 - \alpha(E_K) - \beta(E_K)$ slope around $E_K \simeq 250$ eV and $E_K \simeq 600$ eV. Based on these findings and the assumption that the FRR response function poorly deviates from the expected theoretical energy dependence, the two representative groups have been analysed with (i) constant α_0 exponent (Eq. 5) and (ii) the *ad hoc* change of $\alpha(E_K)$ exponent as given by Eq. 6. The latter parametrization gives a more meaningful description of the observed change of slope at high kinetic energy than a simple polynomial (Eq. 5). But to avoid increasing the number of free parameters, the $E_K \lesssim 200$ eV range that would require a more involved $R(E_K)$ expression was excluded from the analysis as the studied materials does present interesting transitions at those energies.

4.3. Application to experimental data

First, the response function representative of group (A) of Fig. 4 was recovered from the spectrum of the EA-125 analyser working in FAT mode with $6 + 3 \times 10$ mm^2 slits. For all tested metals (Ag, Cu, Au, Zn) covering a wide range of kinetic energies of core levels and Auger transitions, the algorithm converged readily towards an $\alpha_0 = 1.0 \pm 0.1$ exponent (Fig. 5); no clear improvement could be obtained with a polynomial exponent (not shown). As pointed in the analysis of $\mathcal{R}(E_K)$ (Fig. 4), better results are obtained if the kinetic range below ~ 200 eV is excluded from the analysis. Thus, this analyser follows a perfect behaviour in FAT mode as already shown in Refs. [13, 34] but in FRR mode (Fig. 6(a)), the exponent differs from one ($\beta_0 = 0.8 \pm 0.1$) leading to the slight slope observed in $\mathcal{R}(E_K)$ (see Fig. 4).

Treating the second behaviour group (B) observed in the EA-125 response function is more challenging. It is illustrated by the Ag case with $6+5\times11$ mm^2 slits (Fig. 6(b)). As suspected from the analysis of $\mathcal{R}(E_K)$ (Fig. 4), a better convergence for FAT mode spectrum is achieved with the more constrained expression Eq. 6 for $\alpha(E_K)$ than with a simple polynomial (Eq. 5) owing to the physical

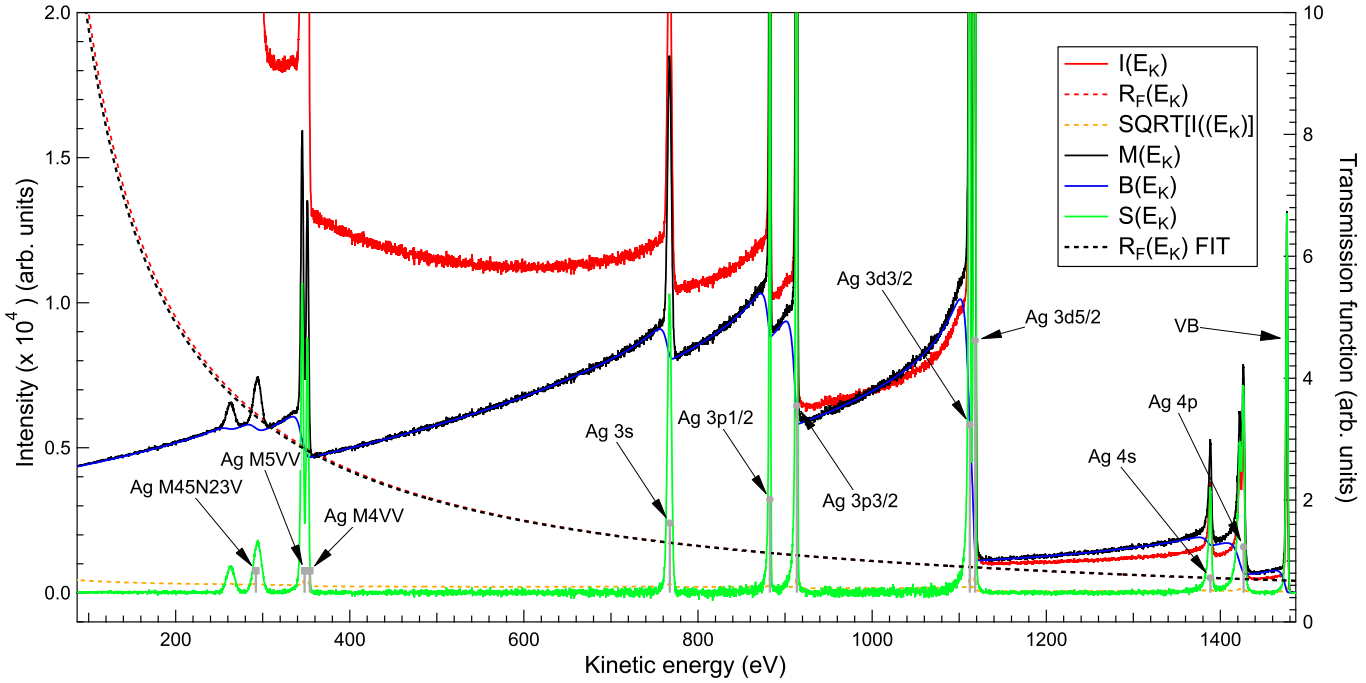

Figure 2: Application of the algorithm of response function retrieval with $[\epsilon = 0.001, \kappa = 1]$ to a theoretical Ag wide photoemission spectrum (see text; $h\nu = 1486.6$ eV with no satellites) : (red full line) initial simulated spectrum $I(E_K)$ including the response function and a Poisson noise; (red dotted line) initial response function $R_F(E_K)$; (orange dotted line) estimate of noise $N(E_K) = \sqrt{I(E_K)}$; (black full line) retrieved spectrum $M(E_K)$ corrected from response function; (blue full line) three-parameter Tougaard background $B(E_K)$; (green full line) retrieved primary spectrum $S(E_K)$; (black dotted line) retrieved response function. Vertical violet sticks correspond to used tabulated core level and Auger line positions.

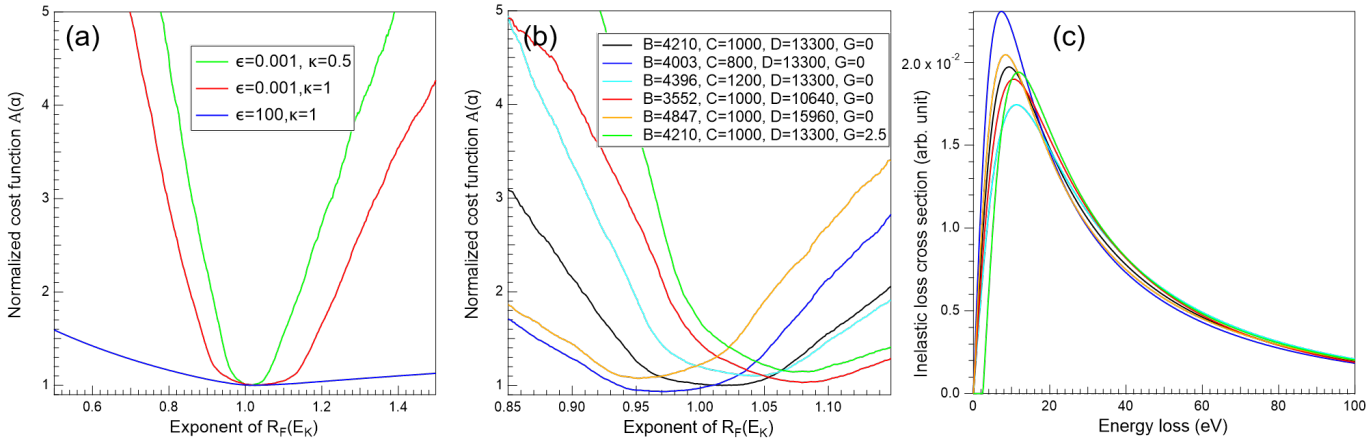

Figure 3: Cost function $\mathcal{A}(\alpha_0)$ (Eq. 7) for a noisy theoretical Ag spectrum as function of the exponent of the response function $R_F(E_K) = 1/E_K^{\alpha_0}$ (a) for several penalty cost parameters $[\epsilon, \kappa]$ (see text for definition) at fixed Tougaard cross section $[B = 4200$ eV^2, $C = 1000$ eV^2, $D = 13300$ eV^2, $G = 0$ eV$]$ (Eq. 3) and (b) for variable $[B, C, D]$ parameters at fixed $[\epsilon = 0.001, \kappa = 0.5]$. The corresponding inelastic electron scattering cross sections are plotted in figure (c) with the same color code as in (b).

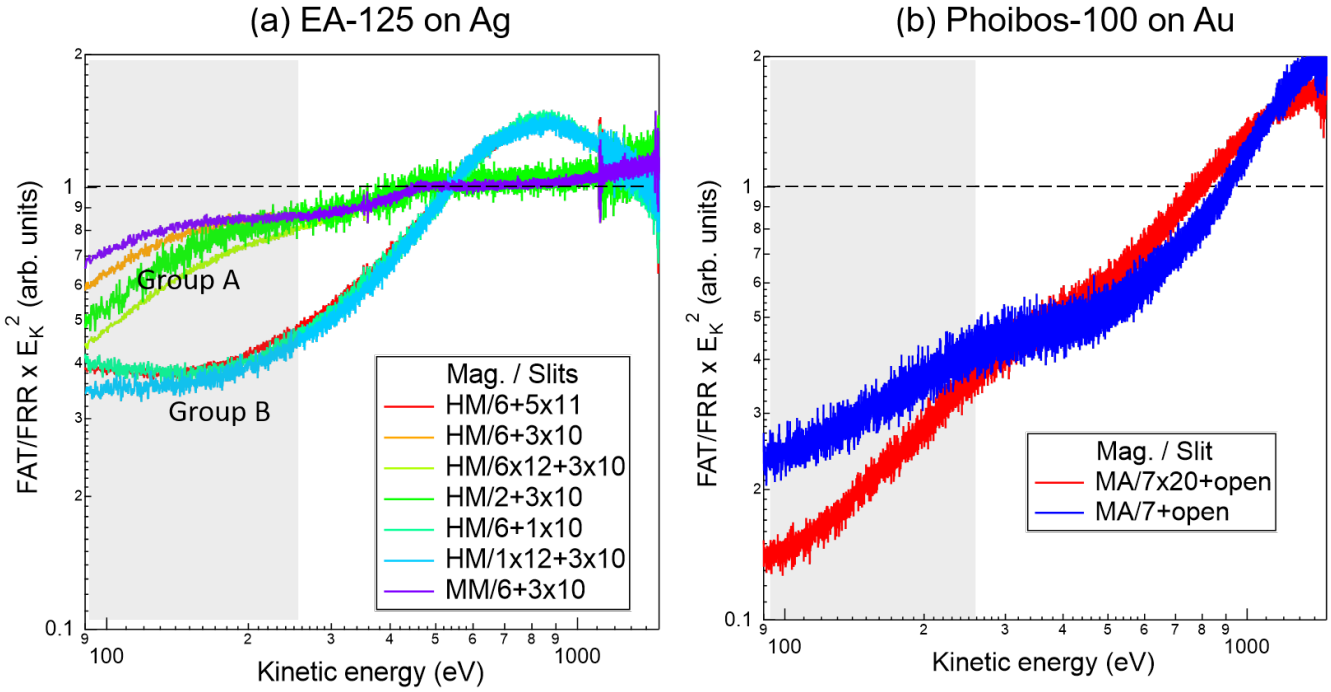

Figure 4: Ratio $\mathcal{R}(E_K) = E_K^2 I_{FAT}(E_K)/I_{FRR}(E_K)$ of spectra acquired in FAT and FRR modes with (a) the EA-125 apparatus ($E_p = 50$ eV; $R = 15$; unmonochromated Al-Kα) on Ag and (b) the Phoibos-100 apparatus ($E_p = 50$ eV; $R = 28$; monochromated Al-Kα) on Au. The dotted line stands for the behaviour of a perfect analyser. The most intense features in spectra give rise to spikes in $\mathcal{R}(E_K)$ since resolution differs between FAT and FRR modes. Different sets of input/output slits and preset magnification modes (HM: high magnification; MM: medium magnification; MA : medium area) are indicated in the figure. For the EA-125 analyser, curves can be gathered into two groups: (A) HM/6 + 3 × 10 mm^2, HM/6 × 12 + 3 × 10 mm^2; HM/2 + 3 × 10 mm^2; MM/6 + 3 × 10 mm^2 and (B) HM/6 + 5 × 11 mm^2, HM/6 + 1 × 10 mm^2, HM/1 × 12 + 3 × 10 mm^2. For the Phoibos-100 analyser, rectangular (7 × 20 mm^2) or circular ($\phi = 7$ mm) input slits have been combined with a fully opened mesh in front of the detector.

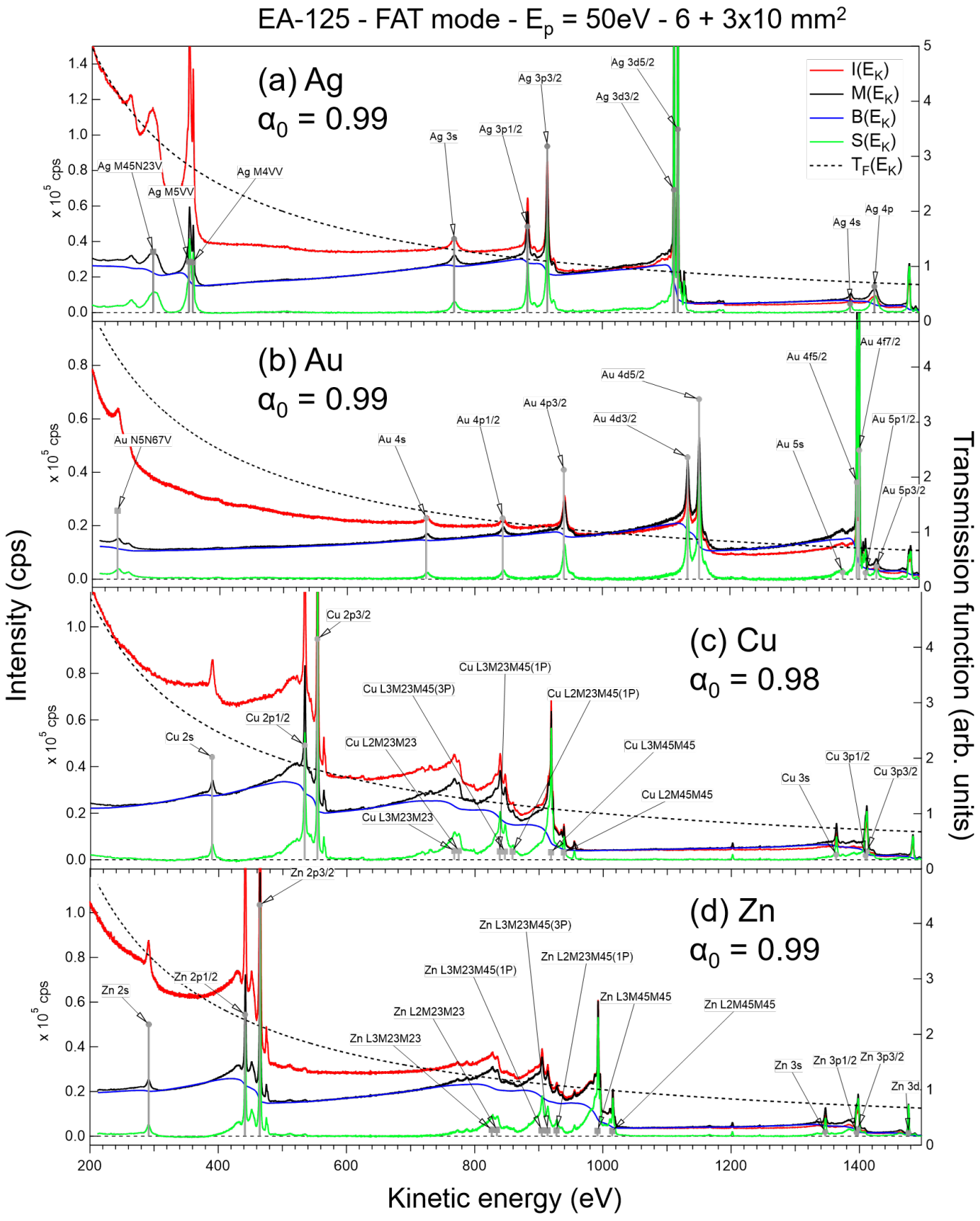

Figure 5: Retrieval [$\epsilon = 0.001; \kappa = 0.5$] of the response function of the EA-125 analyser run in FAT mode ($E_p = 50$ eV) at high magnification with $6 + 3 \times 10$ mm^2 slits from metallic foils: (a) Ag, (b) Cu; (c) Au; (d) Zn. Same labelling as Fig. 2. $R_F(E_K)$ is fitted by a power law $1/E_K^{\alpha_0}$ with a constant exponent given in figure. The x-ray source is a Al-Kα ($h\nu = 1486.6$ eV) unmonochromated tube.

meaning of its parameters in the definition of the starting point of the minimization. The algorithm gave similar values for all metals ($\widetilde{\alpha} \simeq 0.9$, $\Delta\alpha \simeq 0.5$, $E^0_{K,\alpha} \simeq 670$ eV and $\Delta E_{K,\alpha} \simeq 230$ eV). In parallel, the response function in FRR mode with such slits still obeys a power law behaviour with a constant exponent $\beta_0 = 0.9 \pm 0.1$ (Fig. 6(c)). In passing, within small β_0 variation of about 0.1, for this analyser, the quantity $\mathcal{R}(E_K)$ is already a good estimate of the response function of the apparatus in FAT mode.

However, a change of behaviour from case (A) to case (B) can also be observed at fixed slits but variable pass energy (Fig. 7), thus demonstrating a more complex dependence than a simple E_K/E_p scaling in $R_F(E_K)$ as already pointed out in the literature [26, 28, 31, 32]. As seen in Fig. 7(a), this appears as a change from a stair-step background after each core level or Auger lines (case $E_p = 20; 30; 50$ eV) to an unusual decreasing background following each feature (case $E_p = 75; 100$ eV; see also Fig. 6(b)).

Regarding the other analyser, namely the Phoibos-100 with a monochromatic excitation, a similar change in $2 - \alpha(E_K) - \beta(E_K)$ slope is observed in the log-log plot of $\mathcal{R}(E_K)$ (Fig. 4(b)) around $E_K \simeq 600$ eV but between two positive values. Using power law behaviours with exponents given by Eq. 6, the algorithm retrieves similar response functions for all metals for a given set of parameters showing the consistency of the approach (Fig. 8). With a complete reversal from a decreasing to an increasing response function at high kinetic energy when changing from rectangular (Fig. 8(a)) to circular (Fig. 8(b)) slits, $R_F(E_K)$ appears to be more sensitive to slits in FAT mode than in FRR mode. As in the case of the EA-125 analyser, the $R_F(E_K)$-exponent in FRR mode is close to a constant.

4.4. Comparison to theoretical relative sensitivity factors

All the provided examples clearly demonstrate the extreme sensitivity of the response function to working mode, lens magnification, pass energy and slits but also the transferability of the retrieved function from one sample to the other. But, even if results close to previous determination for the EA-125 analyser were obtained [13, 34] the last question is the reliability of the proposed algorithm in terms of quantification compared to tabulated data (Tab. 1). The 19 core level peaks of the obtained primary spectra $S(E_K)$ for all metals and analyser settings, both in FAT and FRR modes, have been directly integrated between fixed limits. Limits have been selected in the nearly zero background level to include K$\alpha_{3,4}$ satellites below the peak if present and all the plasmon and shake-up losses above. For the Au sample, a deconvolution of overlapping Au 5p, Au 4f and Au 5s lines with Doniach-Sunjic profiles at fixed theoretical branching ratios and spin-orbit splittings [59–61] was necessary. The obtained areas have been plotted in Fig. 7(c) and Fig. 9 as a function of the product (Tab. 1) of (i) the photo-ionisation cross section of the considered core level $\frac{d\sigma}{d\Omega} = \sigma^*(h\nu, E_K)W(h\nu, E_K, \theta_X)$ [15] taking into account asymmetry factor if needed and (ii) the inelastic mean free path $\lambda(E_K)$ obtained from the TPP-2M formula at the corresponding kinetic energy [17, 22]. No correction from elastic scattering [4, 5, 8, 9] was accounted for as, for a homogeneous sample, it was found to be overshadowed by the uncertainties in σ^* and λ in the quantification except for of thin layers buried at large depths [62, 63]. Experimental areas and theoretical products have been normalised by their respective sums to be able to compare different samples by getting rid (i) of intensity variations from one scan to the other and (ii) of the atomic concentration of each metal (see Eq. 1). In line with Refs. [42, 53, 54] showing the better reliability of the Tougaard background for quantification, the linear correlation of Fig. 7(c) and Fig. 9 fully validates the methodology by exploring a wide range of kinetic energies from 219.6 eV (Zn 2s) to 1429.6 eV (Au 5p) (see Tab. 1 and inset of Fig. 9) and a great variety of response functions provided by different apparatuses working in FAT or FRR modes with different lens and slit settings under (un)monochrotmated excitations. In contrast to the Quantified Peak Area Approach [26, 27, 35, 36], this correlation is not assumed here but a result of the algorithm. Beyond the bias of the method due to the simplified parametrization of the response function, deviations from the linear trend may result from uncertainties in the $\frac{d\sigma}{d\Omega}(E_K)\lambda(E_K)$ theoretical parameters that can reach up to 20 % [14–22] or from the assumption of a homogeneous flat sample described by the Tougaard background. But most importantly, the bunching of all measurements within ± 10 % for each core level reinforces the consistency of the analysis method in very different situations and sets the level uncertainty of the present approach. Even if there is still some room for improvement for the choice of the inelastic scattering cross section, the parametrization of the response function, the minimization algorithm or the chosen penalty in the cost function, the proposed method (Fig. 1) appears quite robust. In passing, its reversed version, based on the knowledge of $R_F(E_K)$, could be used to determined the unknown Tougaard background parameters of a given sample.

5. Conclusion

A method of retrieval of the intensity/energy response function of a photoemission hemispherical analyser based on the measurement of a wide spectrum of a reference metal (Ag, Cu, Au, Zn) has been described. From only the knowledge of the Tougaard cross section of inelastic losses, the parametrized response function is determined by minimizing the area of the primary spectrum with some constraints. The method has been tested successfully both at fixed pass energy and fixed retardation ratio on two different analysers with different lens and slits settings and x-ray source focusing and validated *a posteriori* on tabulated relative sensitivity factors. This study opens interesting perspectives for a rapid intensity calibration of

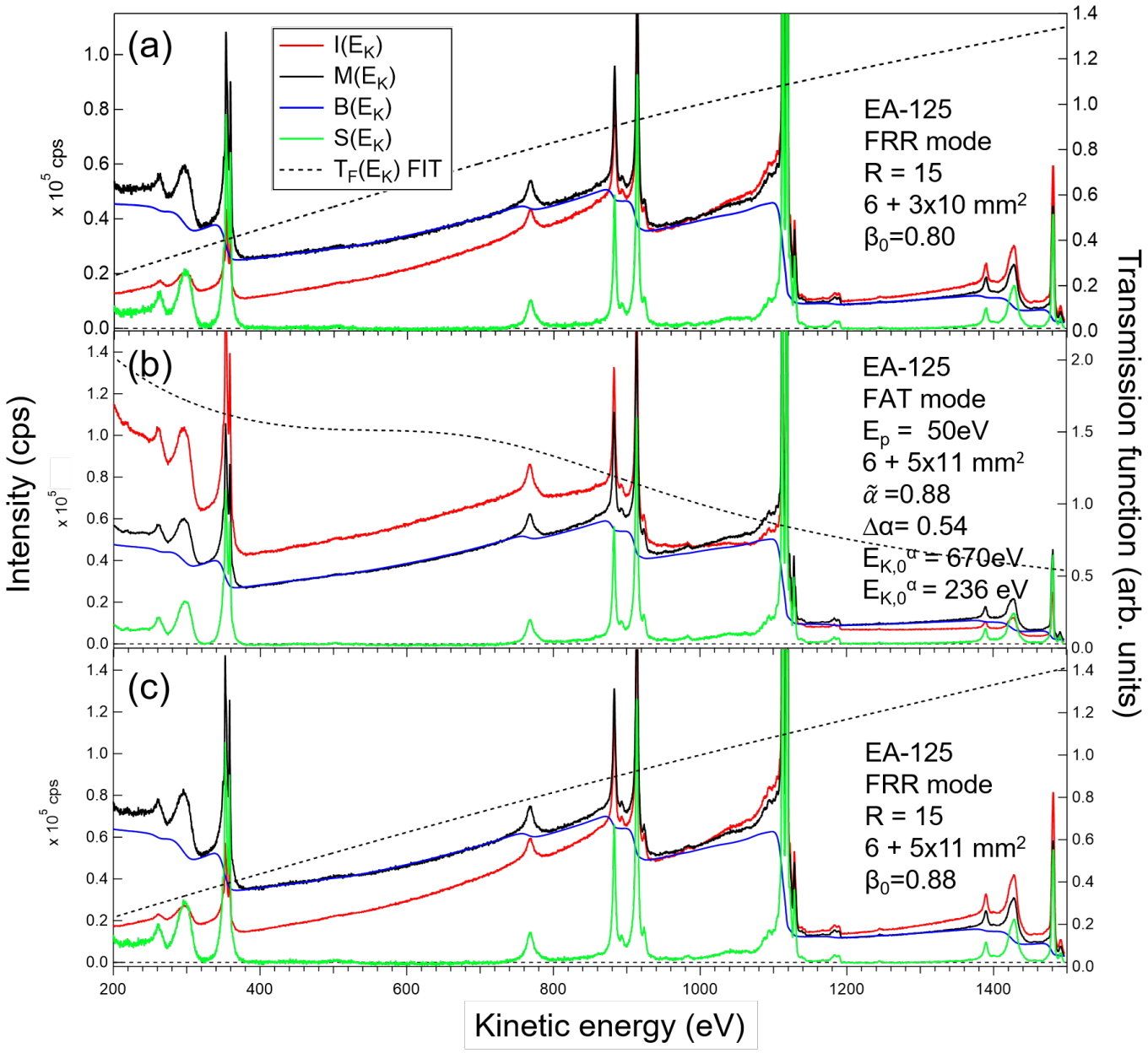

Figure 6: Same as Fig. 5 for Ag : (a) FRR ($R = 15$) mode with $6 + 3 \times 10$ mm^2 slits; (b) FAT ($E_p = 50$ eV) mode with $6 + 5 \times 11$ mm^2 slits; (c) FRR ($R = 15$) mode with $6 + 5 \times 11$ mm^2 slits. Analysis was performed with power laws with a constant exponent ($E_K^{\beta_0}$) or with a $\alpha(E_K)$ exponent given by Eq. 6. Parameters are given in figure.

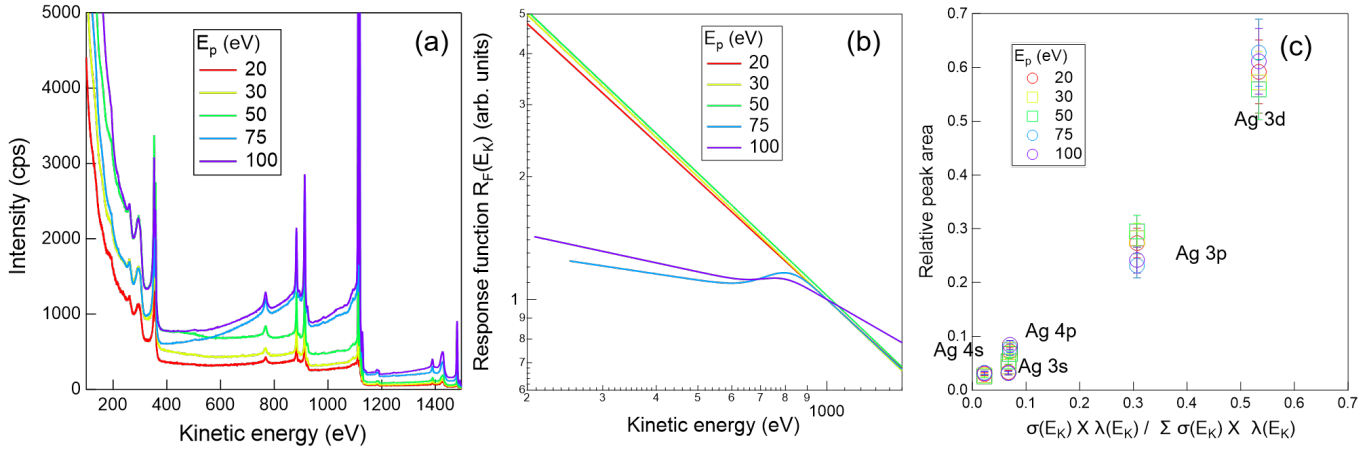

Figure 7: (a) Ag spectra recorded in FAT mode on the EA-125 analyser with fixed $6+3\times10$ mm^2 slits and variable pass energy. (b) Retrieved response functions with Eq. 6. (c) Corresponding core level areas as a function of their theoretical values $d\sigma/d\Omega(h\nu, E_K, \theta_X)\lambda(E_K)$ (values are normalized by the sum; see text for explanation).

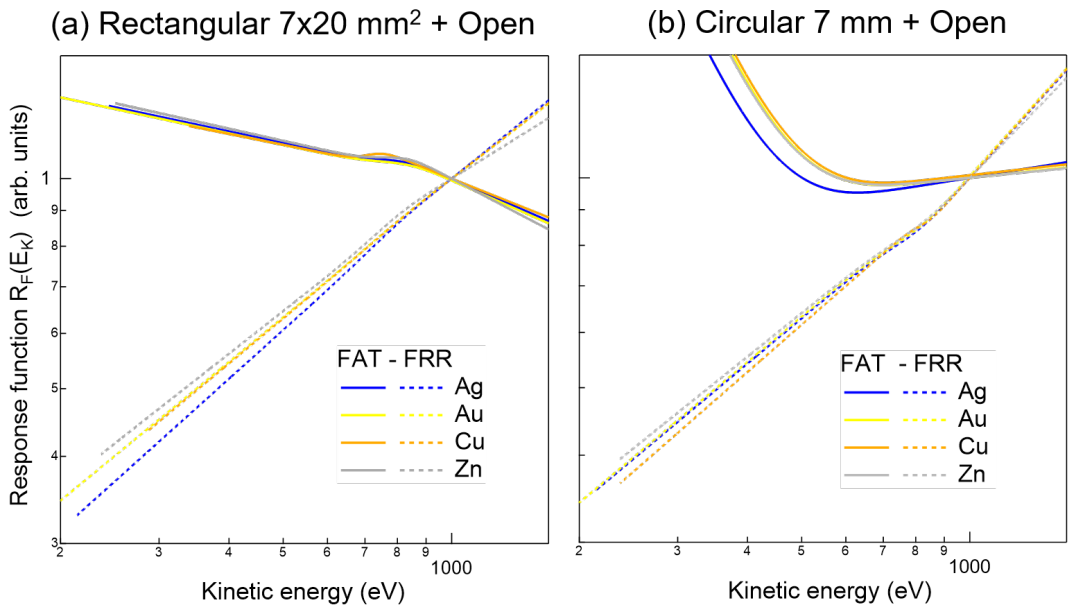

Figure 8: Response function of the Phoibos-100 analyser retrieved from Ag, Au, Cu and Zn wide spectra acquired in FAT ($E_p = 50$ eV; full lines) and in FRR ($R = 22$ for Ag and $R = 28$ for Au, Cu, Zn; dotted lines) modes with a (a) rectangular (7×20 mm^2) and (b) circular ($\Phi = 7$ mm) input slit and a open mesh in front of the detector.

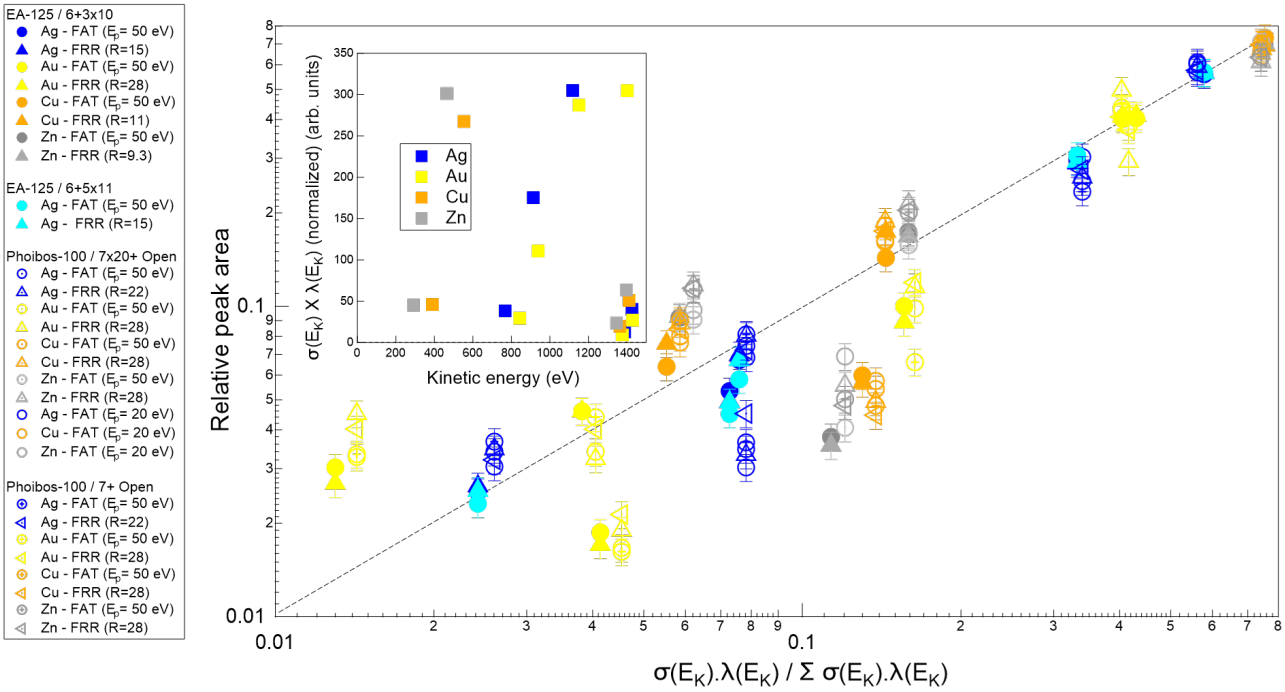

Figure 9: Areas of all core levels for all apparatus, metals and lens/slit settings as a function of their tabulated relative sensitivity factors $\frac{d\sigma}{d\Omega}(h\nu, E_K, \theta_X)\lambda(E_K)$ (see text). For comparison, areas have been normalized to their sum for a given spectrum while, for comparison, the abscissa have been rescaled to the sum of the theoretical relative sensitivity factors of each element. The inset shows the theoretical intensity of the core levels of each element as a function of its kinetic energy. Error bars on experimental areas correspond to 10 %. The dotted curve corresponds to a one-to-one linear trend.

Metal	Level	E_B (eV)	E_K (eV)	$\frac{d\sigma}{d\Omega}$ (norm.)	λ (Å)
				EA125/Phoi100	
Ag	4p	60	1426.6	2.08 / 2.64	19.3
Ag	4s	98	1388.6	0.68 / 0.90	18.9
Ag	3d	368.3	1118.3	19.03 / 22.76	16.0
Ag	3p	573	913.6	12.7 / 16.00	13.8
Ag	3s	719	767.6	3.15 / 4.18	12.2
Au	5p	57	1429.6	1.69 / 2.17	16.0
Au	4f	84	1402.6	19.31 / 22.55	15.8
Au	5s	110	1376.6	0.59 / 0.78	15.6
Au	4d	335	1151.6	21.07 / 25.31	13.6
Au	4p	547	939.6	9.41 / 11.89	11.8
Au	4s	643	843.6	2.69 / 3.57	10.9
Cu	3p	75	1411.6	2.54 / 3.16	20.1
Cu	3s	123	1363.6	1.00 / 1.32	19.6
Cu	2p	932.7	553.9	26.44 / 32.57	10.1
Cu	2s	1097	389.6	5.77 / 7.64	8.0
Zn	3p	89	1397.6	2.84 / 3.55	22.3
Zn	3s	140	1346.6	1.07 / 1.42	21.7
Zn	2p	1021.8	464.8	30.05 / 36.88	10.0
Zn	2s	1195	291.6	6.08 / 8.04	7.5

Table 1: List of parameters of the herein studied core levels: binding energy (E_B), kinetic energy (E_K) for Al-Kα source, photo-ionisation cross sections accounting for asymmetry factor $\frac{d\sigma}{d\Omega}$ (normalized to the C 1s one) for EA-125/Phoibos-100 configurations [15] and TPP-2M inelastic mean free path (λ) [19, 22].

photoemission setups since it requires only the measurement of a wide spectrum of a common reference metallic polycrystalline material and it is not based on the knowledge of the inelastic mean free paths or photo-ionisation cross sections at a limited number of core levels.

Acknowledgements

The authors would like to thank G. Cabailh (INSP) for his careful reading of the manuscript and all members of "Fédération de Recherche Spectroscopie de Photoémission" (FR 2050 CNRS) for fruitful discussions.

References

[1] S. Hofmann, Auger-and X-ray photoelectron spectroscopy in materials science: a user-oriented guide, Vol. 49, Springer Science & Business Media, 2012.

[2] A. G. Shard, Detection limits in XPS for more than 6000 binary systems using Al and Mg kα X-rays, Surf. Interface Anal. 46 (2014) 175–185.

[3] C. S. Fadley, R. J. Baird, W. Siekhaus, T. Novakov, S. A. L. Bergström, Surface analysis and angular distributions in x-ray photoelectron spectroscopy, J. Electron Spectrosc. Relat. Phenom. 4 (1974) 93–137.

[4] A. Jablonski, C. J. Powell, The electron attenuation length revisited, Surf. Sci. Rep. 47 (2002) 33–91.

[5] C. J. Powell, A. Jablonski, NIST electron inelastic mean free path database (2010).

[6] C. R. Brundle, B. V. Crist, X-ray photoelectron spectroscopy: A perspective on quantitation accuracy for composition analysis of homogeneous materials, J. Vac. Sci. Technol., A 38 (2020) 041001.
[7] M. P. Seah, AES and XPS measurements: reducing the uncertainty and improving the accuracy, Appl. Surf. Sci. 70-71 (1993) 1–8.
[8] A. Jablonski, Determination of surface composition by X-ray photoelectron spectroscopy taking into account elastic photoelectron collisions, Analytical Sciences 26 (2010) 155–164.
[9] A. Jablonski, C. J. Powell, Elastic photoelectron-scattering effects in quantitative x-ray photoelectron spectroscopy, Surf. Sci. 606 (2012) 644–651.
[10] M. P. Seah, M. T. Anthony, Quantitative XPS: The calibration of spectrometer intensity-energy response functions. 1-the establishment of reference procedures and instrument behaviour, Surf. Interface Anal. 6 (1984) 230–241.
[11] M. P. Seah, Xps reference procedure for the accurate intensity calibration of electron spectrometers: results of a BCR intercomparison co-sponsored by the VAMAS SCA TWA., Surf. Interface Anal. 20 (1993) 243–266.
[12] M. Kato, T. Sekine, Calculations of a CHA transmission function for quantitative analysis in the constant pass energy mode. i. point sources for AES, Surf. Interface Anal. 21 (1994) 606–614.
[13] M. A. Mahjoub, G. Monier, C. Robert-Goumet, L. Bideux, B. Gruzza, New method for the determination of the correction function of a hemisperical electron analyser based on elastic electron images, J. Electron Spectrosc. Relat. Phenom. 197 (2014) 80–87.
[14] J. H. Scofield, Theoretical photoionization cross sections from 1 to 1500 kev., Technical Report UCRL-51326, Lawrence Livermore Laboratory (1973).
[15] J. Yeh, I. Lindau, Atomic subshell photoionization cross sections and assymetry parameters: $1 \leq z \leq 300$, At. Data Nucl. Data Tables 32 (1985) 1–155.
[16] M. B. Trzhaskovskaya, V. I. Nefedov, V. G. Yarzhemsky, Photoelectron angular distribution parameters for elements $z = 55$ to $z = 100$ in the photoelectron energy range $100 - 5000$ ev, At. Data Nucl. Data Tables 82 (2) (2002) 257–311.
[17] S. Tanuma, C. J. Powell, D. R. Penn, Calculations of electron inelastic mean free paths (IMFPS). IV. Evaluation of calculated IMFPs and of the predictive IMFP formula TPP-2 for electron energies between 50 and 2000 eV, Surf. Interface Anal. 20 (1993) 77–89.
[18] C. J. Powell, A. Jablonski, Evaluation of calculated and measured electron inelastic mean free paths near solid surfaces, J. Phys. Chem. Ref. Data 28 (1999) 19–62.
[19] S. Tanuma, C. J. Powell, D. R. Penn, Calculation of electron inelastic mean free paths (IMFPs) VII. reliability of the TPP-2M IMFP predictive equation, Surf. Interface Anal. 35 (3) (2003) 268–275.
[20] S. Tanuma, T. Shiratori, T. Kimura, K. Goto, S. Ichimura, C. J. Powell, Experimental determination of electron inelastic mean free paths in 13 elemental solids in the 50 to 5000 ev energy range by elastic-peak electron spectroscopy, Surf. Interface Anal. 37 (2005) 833–845.
[21] C. J. Powell, Practical guide for inelastic mean free paths, effective attenuation lengths, mean escape depths, and information depths in x-ray photoelectron spectroscopy, J. Vac. Sci. Technol., A 38 (2020) 023209.
[22] S. Tougaard, QUASES-IMFP-TPP2M Software, http://www.quases.com/products/quases-imfp-tpp2m/.
[23] M. P. Seah, G. C. Smith, Quantitative AES and XPS: Determination of the electron spectrometer transmission function and the detector sensitivity energy dependencies for the production of true electron emission spectra in aes and xps, Surf. Interface Anal. 15 (1990) 751–766.
[24] C. D. Wagner, L. E. Davis, M. V. Zeller, J. A. Taylor, R. H. Raymond, L. H. Gale, Empirical atomic sensitivity factors for quantitative analysis by electron spectroscopy for chemical analysis, Surf. Interface Anal. 3 (1981) 211–225.
[25] Y. M. Cross, J. E. Castle, The relationship between transmission efficiencies in the FRR and FAT modes of an electron spectrometer, J. Electron Spectrosc. Relat. Phenom. 22 (1981) 53 – 60.
[26] L. T. Weng, G. Vereecke, M. J. Genet, P. Bertrand, W. E. E. Stone, Quantitative XPS. part I: Experimental determination of the relative analyser transmission function of two different spectrometers - a critical assessment of various methods, parameters involved and errors introduced, Surf. Interface Anal. 20 (1993) 179–192.
[27] J. Trigueiro, W. Lima, N. Bundaleski, O. M. N. D. Teodoro, XPS spectrometer transmission function optimization by the differential evolution algorithm, J. Electron Spectrosc. Relat. Phenom. 222 (2018) 122–132.
[28] M. P. Seah, Scattering in electron spectrometers, diagnosis and avoidance. I. Concentric hemispherical analysers, Surf. Interface Anal. 20 (1993) 865–875.
[29] K. Richter, B. Peplinski, Determination of relative transmission function of two scanning modes of an electrostatic hemispherical analyser with a lens system, Surf. Interface Anal. 2 (4) (1980) 161–63.
[30] H. Ebel, G. Zuba, M. F. Ebel, A modified bias-method for the determination of spectrometer functions, J. Electron Spectrosc. Relat. Phenom. 31 (1983) 123–130.
[31] C. S. Hemminger, T. A. Land, A. Christie, J. C. Hemminger, An empirical electron spectrometer transmission function for applications in quantitative XPS, Surface and Interface Analysis 15 (1990) 323–327.
[32] J. A. Carrazza, V. León, A general and simple approach for the determination of energy analyser transmission functions, Surf. Interface Anal. 17 (1991) 225–229.
[33] L. Zommer, Determination of the spectrometer transmission function for XPS quantitative analysis, Vacuum 46 (1995) 617–620.
[34] P. Ruffieux, P. Schwaller, O. Gröning, L. Schlapbach, P. Gröning, Q. C. Herd, D. Funnemann, J. Westermann, Experimental determination of the transmission factor for the Omicron EA125 electron analyzer, Rev. Sci. Instr. 71 (2000) 3634–3639.
[35] R. Hesse, P. Streubel, R. Szargan, Improved accuracy of quantitative XPS analysis using predetermined spectrometer transmission functions with UNIFIT 2004, Surf. Interface Anal. 37 (2005) 589–607.
[36] G. Drera, G. Salvinelli, J. Ahlund, P. G. Karlsson, B. Wannberg, E. Magnano, S. Nappini, L. Sangaletti, Transmission function calibration of an angular resolved analyzer for x-ray photoemission spectroscopy: Theory vs experiment, J. Electron Spectrosc. Relat. Phenom. 195 (2014) 109–116.
[37] A. G. Shard, S. J. Spencer, Intensity calibration for monochromated Al Kα XPS instruments using polyethylene, Surf. Interface Anal. 51 (2019) 618–626.
[38] M. P. Seah, A system for the intensity calibration of electron spectrometers, J. Electron Spectrosc. Relat. Phenom. 71 (3) (1995) 191–204.
[39] B. P. Reed, D. J. H. Cant, S. J. Spencer, A. J. Carmona-Carmona, A. Bushell, A. Herrera-Gómez, A. Kurokawa, A. Thissen, A. G. Thomas, A. J. Britton, A. Bernasik, A. Fuchs, A. P. Baddorf, B. Bock, B. Theilacker, B. Cheng, D. G. Castner, D. J. Morgan, D. Valley, E. A. Willneff, E. F. Smith, E. Nolot, F. Xie, G. Zorn, G. C. Smith, H. Yasufuku, J. L. Fenton, J. Chen, J. D. P. Counsell, J. Radnik, K. J. Gaskell, K. Artyushkova, L. Yang, L. Zhang, M. Eguchi, M. Walker, M. Hajdyla, M. M. Marzec, M. R. Linford, N. Kubota, O. Cortazar-Martinez, P. Dietrich, R. Satoh, S. L. M. Schroeder, T. G. Avval, T. Nagatomi, V. Fernandez, W. Lake, Y. Azuma, Y. Yoshikawa, A. G. Shard, Versailles project on advanced materials and standards interlaboratory study on intensity calibration for x-ray photoelectron spectroscopy instruments using low-density polyethylene, J. Vac. Sci. Technol., A 38 (2020) 063208.
[40] H. M., A. Lippitz, R. Hesse, R. Denecke, W. S. M. Werner,

W. E. S. Unger, The use of ionic liquids for the determination of the spectrometer transmission function in x-ray photoelectron spectroscopy (XPS), J. Electron Spectrosc. Relat. Phenom. 233 (2019) 51–56.
[41] A. G. Shard, Practical guides for x-ray photoelectron spectroscopy: Quantitative XPS, J. Vac. Sci. Technol., A 38 (2020) 041201.
[42] M. H. Engelhard, D. R. Baer, A. Herrera-Gomez, P. M. A. Sherwood, Introductory guide to backgrounds in XPS spectra and their impact on determining peak intensities, J. Vac. Sci. Technol., A 38 (2020) 063203.
[43] https://scientaomicron.com/en.
[44] https://www.specs group.com/.
[45] S. Tougaard, P. Sigmund, Influence of elastic and inelastic scattering on energy spectra of electrons emitted from solids, Phys. Rev. B 25 (1982) 4452–4466.
[46] S. Tougaard, Quantitative analysis of the inelastic background in surface electron spectroscopy, Surf. Interface Anal. 11 (9) (1988) 453–472.
[47] S. Tougaard, Universality classes of inelastic electron scattering cross-sections, Surf. Interface Anal. 25 (3) (1997) 137–154.
[48] S. Tougaard, Energy loss in XPS: Fundamental processes and applications for quantification, non-destructive depth profiling and 3D imaging, J. Electron Spectrosc. Relat. Phenom. 178-179 (2010) 128 – 153.
[49] S. Tougaard, Practical algorithm for background subtraction, Surf. Sci. 216 (3) (1989) 343–360.
[50] M. P. Seah, Background subtraction: I. General behaviour of Tougaard-style backgrounds in AES and XPS, Surf. Sci. 420 (2) (1999) 285 – 294.
[51] E. Gnacadja, N. Pauly, S. Tougaard, Universal inelastic electron scattering cross-section including extrinsic and intrinsic excitations in XPS, Surf. Interface Anal. 52 (2020) 413–421.
[52] S. Tougaard, Background removal in x-ray photoelectron spectroscopy: Relative importance of intrinsic and extrinsic processes, Phys. Rev. B 34 (1986) 6779–6783.
[53] M. Repoux, Comparison of background removal methods for xps, Surf. Interface Anal. 18 (1992) 567–570.
[54] S. Tougaard, C. Jansson, Comparison of validity and consistency of methods for quantitative xps peak analysis, Surf. Interface Anal. 20 (13) (1993) 1013–1046.
[55] R. Lazzari, `Igor Pro Paris Photoemission Package` can be downloaded with a user guide from: http://www.insp.upmc.fr/I4P-Igor-Pro-Paris-Photoemission.html?lang=en.
[56] https://www.wavemetrics.com/.
[57] J. E. Dennis, R. B. Schnabel, Numerical methods for unconstrained optimization and nonlinear equations, 1987.
[58] A. Corana, M. Marchesi, C. Martini, S. Ridella, Minimizing multimodal functions of continuous variables with the Simulated Annealing Algorithm - corrigenda for this article is available here, ACM Trans. Math. Softw. 13 (3) (1987) 262–280.
[59] C. D. Wagner, W. M. Riggs, L. E. Davis, J. F. Moulder, G. E. Muilenberg, Handbook of X-Ray Photoelectron spectroscopy, Perkin-Elmer, Eden Prairie, 1979.
[60] J. F. Moulder, W. F. Stickle, P. E. Sobol, K. D. Bomben, Handbook of X-ray photoelectron spectroscopy, Physical Electronics, Perkin Elmer., Eden Prairie, Minnesota, USA, 1995.
[61] NIST X-ray photoelectron spectroscopy database, https://srdata.nist.gov/xps/Default.aspx.
[62] S. Tougaard, A. Jablonski, Test of elastic electron scattering corrections for quantitative XPS, Surface and Interface Analysis 23 (1995) 559–564.
[63] S. Tougaard, A. Jablonski, Quantitative XPS: Influence of elastic electron scattering in quantification by peak shape analysis, Surf. Interface Anal. 25 (1997) 404–408.